

# Photochemically Engineered Large-Area Arsenic Sulfide Micro-Gratings for Hybrid Diffractive–Refractive Infrared Platforms

Myungkoo Kang,\* Brandon M. Triplett, Mikhail Y. Shalaginov, Skylar Deckoff-Jones, Cesar Blanco, Mia Truman, Elena Shirshneva-Vashchenko, Justin Cook, Qingyang Du, Tushar S. Karnik, Cosmin-Constantin Popescu, Anna Zachariou, Yifei Zhang, Casey M. Schwarz, Sensong An, Clayton Fowler, Hualiang Zhang, Ivan Divliansky, Leonid B. Glebov, Martin C. Richardson, Anuradha M. Agarwal, Clara Rivero-Baleine, Juejun Hu, Tian Gu,\* and Kathleen A. Richardson


Patterns composed of micron-sized surface structures can abruptly change the properties of an optical wave front, including its phase, amplitude, polarization, and dispersion. Optical components featuring surface micro-gratings not only possess optical functionalities that can rival or exceed those of traditional bulky components but can also significantly improve the compactness of optical systems. Herein, the design and fabrication process of As<sub>2</sub>S<sub>3</sub> glass-based micro-gratings as well as their resulting optical functionality in the infrared regime are reported. The novel two-step photochemical process consists of spatially controlled direct laser writing and subsequent selective solution etching. The process yields surface micro-gratings that possess arbitrarily tunable geometries and design patterns on large-area flat and curved optical surfaces or substrates, offering a potential new avenue for developing aberration-corrected infrared-imaging systems.

## 1. Introduction

Diffraction gratings were first introduced by Rittenhouse,<sup>[1]</sup> theoretically established by Rowland,<sup>[2]</sup> and commercially manufactured by Richardson and Wiley.<sup>[3]</sup> Diffraction gratings have become a fundamental and indispensable optical component due to their ability to separate polychromatic light into its constituent monochromatic components.<sup>[4]</sup> The wide tunability of the diffraction grating's unit cell offers additional degrees of freedom over conventional materials, which are governed solely by material composition, for achieving specific target properties in many demanding optical, electronic, and magnetic applications.<sup>[5–10]</sup> The extremely high precision demanded by diffraction gratings

of scientific and technical value has pushed fabrication technology to its limits to develop increasingly precise grating structures for a diverse range of materials.<sup>[4]</sup> However, the majority of

M. Kang,<sup>[†]</sup> C. Blanco, E. Shirshneva-Vashchenko, J. Cook, A. Zachariou, I. Divliansky, L. B. Glebov, M. C. Richardson, K. A. Richardson  
CREOL, College of Optics and Photonics  
University of Central Florida  
Orlando, FL 32816, USA  
E-mail: kangm@alfred.edu

 The ORCID identification number(s) for the author(s) of this article can be found under <https://doi.org/10.1002/adpr.202300241>.

<sup>[†]</sup>Present address: Ceramic Engineering Program, Alfred University, Alfred, NY 14802, USA

<sup>[††]</sup>Present address: School of Electrical Engineering and Computer Science, Purdue University, West Lafayette, IN 47907, USA

© 2023 The Authors. Advanced Photonics Research published by Wiley-VCH GmbH. This is an open access article under the terms of the Creative Commons Attribution License, which permits use, distribution and reproduction in any medium, provided the original work is properly cited.

DOI: 10.1002/adpr.202300241

B. M. Triplett,<sup>[††]</sup> C. Rivero-Baleine  
Missiles and Fire Control  
Lockheed Martin Corporation  
Orlando, FL 32819, USA

M. Y. Shalaginov, S. Deckoff-Jones, Q. Du, T. S. Karnik, C.-C. Popescu, Y. Zhang, A. M. Agarwal, J. Hu, T. Gu  
Department of Materials Science and Engineering  
Massachusetts Institute of Technology  
Cambridge, MA 02139, USA  
E-mail: gutian@mit.edu

M. Truman, C. M. Schwarz  
Department of Physics and Astrophysics  
Ursinus College  
Collegeville, PA 19426, USA

S. An, C. Fowler, H. Zhang  
Department of Electrical Engineering and Computer Science  
University of Massachusetts Lowell  
Lowell, MA 01854, USA

current techniques are limited to planar platforms, which involve complex multistep processes.<sup>[5–10]</sup> The optimization of a fabrication process that is compatible with nonplanar platforms has been increasingly necessary since spectral aberrations, typically lingering in refractive optics, can be significantly mitigated by adding an optically engineered diffractive optics layer onto the curved surface of the refractive component.<sup>[11]</sup> Such a conformal fabrication method becomes challenging due to requirements such as high spatial resolution, process scalability, applicability to a wide range of material systems, and performance across a range of spectral windows.

The first step in many surface micro-grating fabrication techniques is writing a spatial mask, followed by a selective material removal process (reactive ion etching or liftoff). Mask writing processes capable of fabricating spatially patterned 3D structures include electron-beam lithography,<sup>[12–15]</sup> ion-beam-induced preferential sputtering,<sup>[16–18]</sup> and direct laser writing (DLW).<sup>[19–21]</sup> The DLW process has three unique advantages over electron and ion beam-based processes in material modification. First, both electron and ion irradiation processes require a vacuum to be reached to avoid collision with ambient molecules. The DLW process does not necessitate a vacuum chamber. This vacuum-free standalone mode enables target samples to be irradiated in a variety of spatial configurations such as by using fully rotatable or tiltable stations, which facilitate conformal DLW on curved surfaces. Second, electron-beam lithography typically requires target samples to be conductive and electrically grounded to avoid charging effects, which often lead to loss of patterning accuracy. The DLW process does not have such a restriction and hence is applicable to a wide range of material systems. Third, ion irradiation implants external elements into target materials that alter parent media stoichiometry and often form various types of structural defects. The DLW process when employed with sub-ablation intensity thresholds can serve as a compositionally preserving, nondestructive method to create gratings. Additionally, DLW is particularly amenable to rapid prototyping of new designs for large-scale components, thus making its capital cost favorable over electron and ion beam processes. Specifically, key advantages of recent commercial laser writing systems (such as those from Heidelberg Instruments, Femtika, Nanoscribe, and UpNano) include large areas ( $\sim 100\text{ cm}^2$ ), fast ( $\sim \text{mm}^2\text{ min}^{-1}$ ), decent resolution ( $\sim$ hundreds of nm), material agnostic (in case of ablation), and 3D shapes (requires photosensitive polymers).

Chalcogenide glasses have been attractive target materials for the DLW process due to their unique sub-ablation laser–matter interactions, which can be utilized to convert them into spatially ordered structures with novel properties.<sup>[22–26]</sup> Near-bandgap laser exposure of target chalcogenide glasses often induces the excitation of their lone-pair electrons or in some cases defects, which in turn leads to the reorganization of atomic bond structures.<sup>[22–26]</sup> The resulting material modification has been shown to be composition and form specific (bulk, films, or fibers), and is dictated largely by the type of bonding present in the irradiated material. The types of atomic reorganization observed in a laser-exposed volume of chalcogenide glasses typically include severing and/or cross-linking of bonds over an interatomic length scale and the migration of atoms, which can result in phase separation over a relatively longer length

scale.<sup>[22–26]</sup> The laser-induced cross-linking, sometimes called polymerization, of atomic bonds in chalcogenide glasses was first reported in pioneering work by Zoubir et al.,<sup>[26]</sup> in which the unique phenomenon was further utilized to create waveguide structures embedded in  $\text{As}_2\text{S}_3$  chalcogenide glasses through spatially controlled DLW process. This work was further extended by Schwarz and coworkers who aimed to make metastructures in the form of pillars in  $\text{As}_2\text{S}_3$  films.<sup>[27]</sup> Importantly, both studies, while different in target geometries (waveguides versus pillars), show that laser-written chalcogenide glasses possessing a spatially varying extent of atomic cross-linking imparted by laser writing exhibit structures that differ from an unexposed material. Such spatial variation of the glass network makes the glass suitable for possible subsequent processing whereby surface 3D microstructures can be realized.

Inspired by these studies and employing further advances in DLW protocols, we utilize a novel photochemical method, consisting of DLW and post selective etching processes, to fabricate spatially tailorable large-area conformal  $\text{As}_2\text{S}_3$  surface micro-gratings. We employ a synergistic approach combining computation-guided design and experimental demonstration to assess the performance of surface grating-based diffractive optical elements (DOEs) toward the realization of aberration-free lightweight hybrid diffractive–refractive infrared media.

## 2. Versatile Two-Step Photothermal Surface Micro-Grating Fabrication Process

Figure 1a illustrates a schematic of the photothermal process employed in our micro-grating fabrication.  $\text{As}_2\text{S}_3$  chalcogenide glasses are prepared using a standard lab-scale melt-quench protocol to serve as target source materials for thermal evaporation and deposition onto ZnSe substrates.<sup>[28]</sup> As-deposited  $\text{As}_2\text{S}_3$  layers are then subjected to near-bandgap femtosecond laser beam writing with a center wavelength of 801 nm and estimated beam spot diameters of  $D = 1.22\lambda/\text{NA} \approx 1.8\ \mu\text{m}$  and  $\approx 1.3\ \mu\text{m}$  for the  $50\times$  and  $100\times$  objectives used, respectively. Systematic choices of sub-ablation laser powers, focal depths, dwell times, step sizes, and movement patterns were made to induce cross-linking of atomic bonds along spatially defined volumes with various geometries in the layers. The cross-linking of atomic bonds is a direct outcome of laser exposure and determines the post selective etching behavior. Successful cross-linking is clearly indicated by comparing two Raman spectra collected from as-deposited and post-irradiated  $\text{As}_2\text{S}_3$  layers (Figure 1b). Here, the intensity of the low-frequency vibrational bands from 175 to  $250\text{ cm}^{-1}$  substantially decreases upon laser exposure, indicating structural modifications of the molecular arrangement in the layers. The bands existing in as-deposited  $\text{As}_2\text{S}_3$  layers correspond to homopolar  $\text{As}_4\text{S}_4$  molecular clusters.<sup>[26]</sup> The decrease in intensities of these vibrational modes reveals that the near-bandgap laser exposure caused the  $\text{As}_4\text{S}_4$  molecular clusters to reorganize or cross-link and begin to form a glass network similar to that in a melt-quenched bulk, thereby making the region structurally resistant against chemical dissolution.

Following laser writing, the laser-processed samples were submerged into a chemical solvent to selectively dissolve unexposed regions, thereby leaving a laser-written atomically polymerized

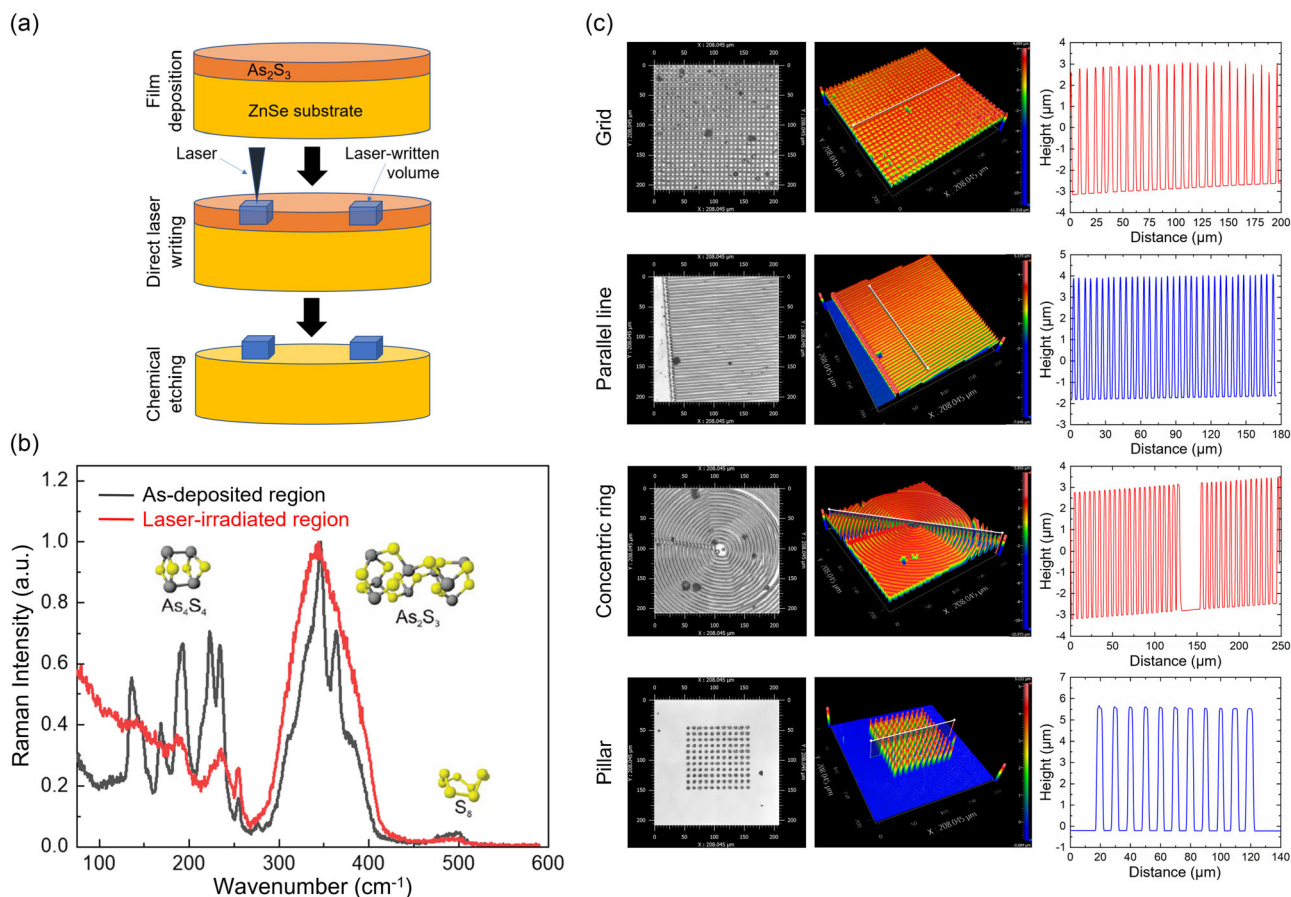


**Figure 1.** a) A schematic of the photochemical process. b) Raman intensities of  $\text{As}_2\text{S}_3$  films before and after laser irradiation. c) A variety of white-light interferograms (WLI) and corresponding cross-section profiles of the surface micro-grating structures including grids, parallel lines, concentric rings, and pillars.

volume behind and creating 3D vertical surface structures. For the choice of solvents in the post selective etching process, it has been reported that polar solvents with high basicity are capable of dissolving sulfide chalcogenide glasses.<sup>[29,30]</sup> Notable examples demonstrated to date include a mixture of di-isopropylamine (DIPA) and dimethyl sulfoxide (DMSO) for the dissolution of  $\text{As}_2\text{S}_3$  films deposited using thermal evaporation process.<sup>[31,32]</sup> Here, a key criterion for their mixing ratio in our study is an ability for a resulting solvent to dissolve as-deposited  $\text{As}_2\text{S}_3$  films in a spatially homogeneous, timely, and structurally selective (laser-exposed vs laser-unexposed) fashion. Specially, DIPA and DMSO must be homogeneously mixed to enable spatially uniform and reproducible dissolution of unexposed regions of films within a reasonable duration. Our matrix experiment consisting of DIPA's mol% and etching duration revealed that  $\approx 0.9$  mol% of DIPA in DMSO is a threshold fraction to induce a phase separation while sub-threshold fractions ranging from 0.4–0.6 mol% of DIPA enable the complete removal of unexposed regions as well as the structural fidelity of resulting surface micro-gratings in less than an hour. Specific parameters for film deposition, laser writing, and post chemical processes are described in Experimental Section.

### 3. Photochemically Patterned Surface Micro-Gratings

Four representative types of surface micro-gratings including grids, parallel lines, concentric rings, and pillar arrays were created over large areas to assess the spatial resolution of individual features within each type of structure as well as their spatial homogeneity across entire areas. Figure 1c shows 3D white-light interferometer (WLI) images of the surface micro-gratings along with their corresponding cross-section profiles depicting features of various shapes and sizes. A closer look at individual walls within surface micro-gratings reveals further insights into the impact of our photochemical process on  $\text{As}_2\text{S}_3$  layers. Figure 2a shows WLI images of grid patterns as an example where the spacing is decreased from 20 to 5  $\mu\text{m}$  while holding all other laser writing parameters constant. Here, the goal was to maintain the shape and dimensions of the resulting individual walls. Figure 2b,c shows cross-section profiles and their zoomed views extracted from the WLI images of the four surface micro-gratings. The cross-sectional area of the grating lines has a shape of a truncated pyramid (sidewall slope of  $\approx 3.6$ ) with a height identical to the thickness of the as-deposited  $\text{As}_2\text{S}_3$

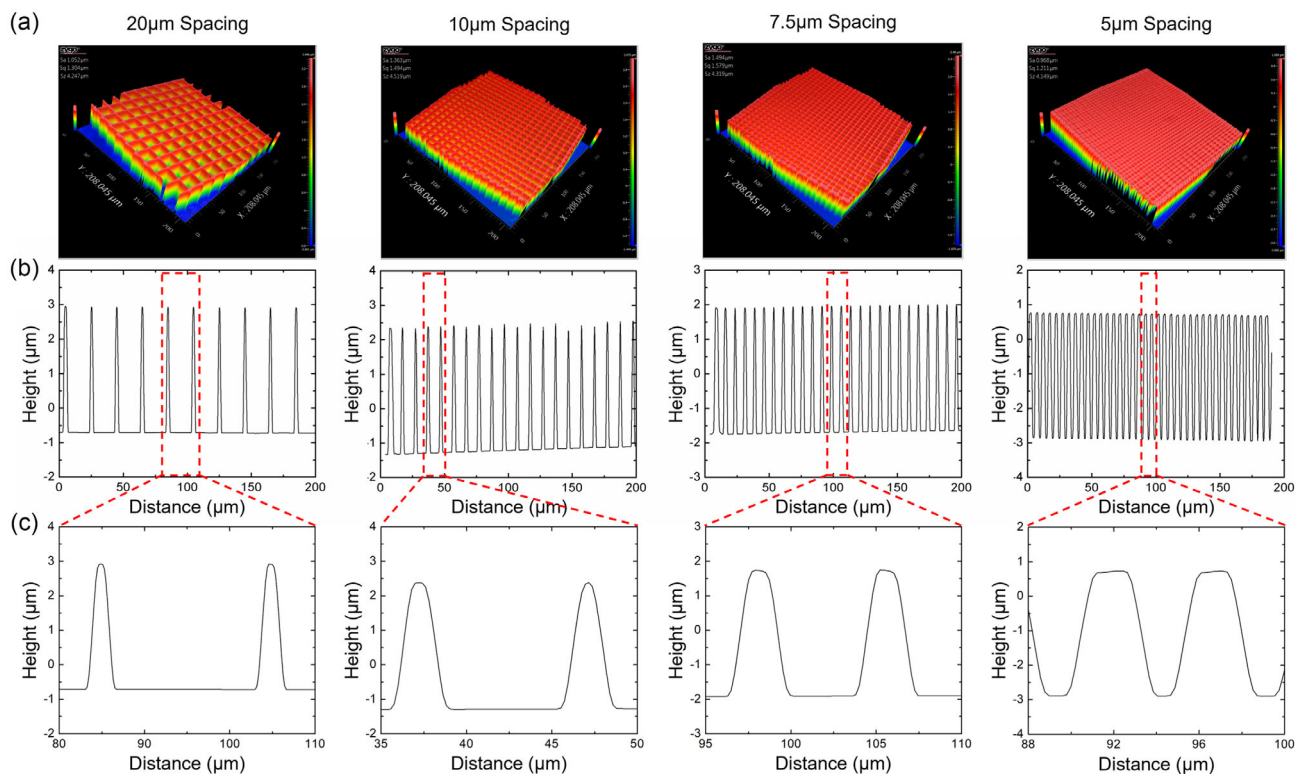


**Figure 2.** a) WLI of grid micro-gratings with varied spacings. b) Cross-section profiles extracted from the WLI images. c) Magnified views of the profiles.

layers (3.5 µm), as shown in Figure 2c. Each line corresponds to a volume with cross-linked atomic bonds, which are induced by laser exposure, indicating that the vertical wall is reminiscent of the laser beam shape inside the film. The focal point of the laser beam is positioned at the surface of the layers for this specific set of grid arrays. As illustrated in Figure 3a, the laser beam converges until it reaches the surface of the layer and diverges while going fully through the layer, thereby forming a beam shape of a truncated cone in 3D space with a height of 3.5 µm. We find that micron-sized features with spacing above approximately 5 µm are realizable over a wide range of length scales and shapes. For example, increased laser power, decreased write speed, or sequential DLW with intentional beam overlap between passes would increase the cross-linked film volume and lead to an increase in the width of the top and bottom bases of individual features. Also, the usage of an objective with a different value of numerical aperture (NA) changes the divergence angle of incident beam, thereby expecting to correspondingly and controllably alter the slope of resulting features' sidewall.

The top width, bottom width, and height of the truncated pyramid, defined in Figure 3a, were extracted from the cross-section profiles in Figure 2b and statistically plotted as a function of wall to wall spacing in Figure 3b. Interestingly, the wall dimensions remain consistent when the spacing exceeds 10 µm, but they change as the spacing is reduced below 10 µm. Figure 3c shows a schematic of intensity profiles of neighboring laser beams. The Gaussian tails of each beam become increasingly overlapped

as the spacing is reduced. The width increase for short-spaced walls is likely attributed to the overlapped laser intensities from separate laser passes, which are intense enough to induce cross-linking of atomic bonds. Our hypothesis is supported by our observation that the walls widen under increased laser power ( $\propto$  intensity), as shown in Figure 3d. This increases the intensity of the Gaussian tails and expands the cross-linked volume. This undesired expansion of cross-linked volume at small spacing leads to feature to feature spacing below 5 µm having inconsistent or poor etching contrast, which limits our optical functionality to the mid-infrared regime. To potentially increase resolution, we suggest using a lower NA objective, which has a smaller divergence angle. This would minimize the overlap of the Gaussian tails of the laser beam and keep the widths of individual walls consistent and more vertical.

#### 4. Conformal Manufacturability

One of the promises of our photochemical process is its applicability to curve or arbitrarily shaped optical surfaces or platforms. A key prerequisite to this capability is to maintain the incidence angle of the laser beam while scanning through a topographically nonuniform surface. Our DLW process is enabled by our fully programmable laser writing stage that can perform high resolution motion in 6 degrees of freedom for precise translation, pitch, yaw, and roll. We program the stage to scan through a topographically nonuniform surface while maintaining a desired

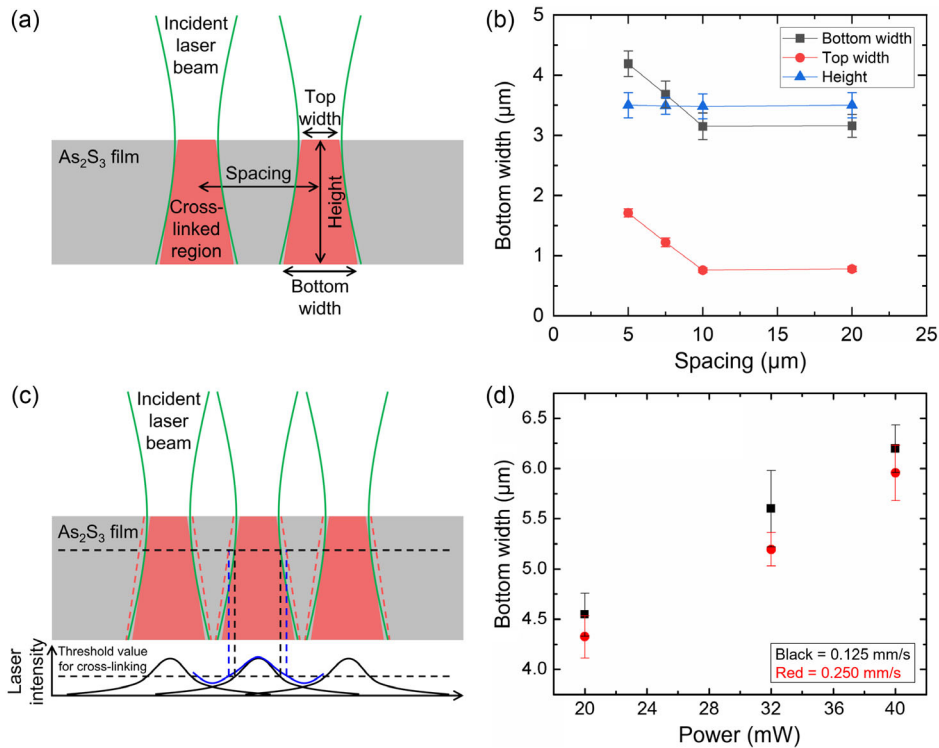


**Figure 3.** a) A schematic of the laser–matter interaction. b) Spacing-dependent variation in the bottom width, top width, and height of individual walls. c) Overlapping of laser–matter interaction volumes and resulting expansion of individual walls' volume. d) Laser-power-dependent width of individual walls.

angle of incidence angle of laser beam such that it is compatible with writing on curved or arbitrarily shaped surfaces. To demonstrate the conformal manufacturability of our photochemical process, we laser wrote 15 μm spaced concentric rings within 2 μm thick As<sub>2</sub>S<sub>3</sub> layers deposited on the surface of ZnSe plano-convex lenses with a diameter of 12.7 mm and a radius of curvature of 56.1 mm. **Figure 4a–d** shows photographs of the As<sub>2</sub>S<sub>3</sub>-coated ZnSe lens, top-view optical + 3D WLI images of photochemically patterned concentric ring structures, and corresponding lateral height profiles of the structures in various locations. The resulting micro-gratings span over the area of interest and exhibit good spatial homogeneity, with an average height of  $1.92 \pm 0.06 \mu\text{m}$  and an average ring-to-ring distance of  $15.03 \pm 0.02 \mu\text{m}$ . The measured height is nearly identical to the thickness of the deposited As<sub>2</sub>S<sub>3</sub> layer; the spacing is as intended in the patterned design. The spatial homogeneity and fabrication precision demonstrate the compatibility of our novel laser-based process with curved substrates for the first time.

## 5. Optical Functionalization as Diffractive–Refractive Infrared Media

Refractive optical elements (ROEs) typically exhibit a positive refractive index dispersion, leading to a decrease in focal length with an increase in wavelength.<sup>[33,34]</sup> To mitigate this issue, a wide variety of methods have been employed to date, such as gradient refractive index (GRIN) media. A curved or predefined

trajectory of electromagnetic waves passing through a GRIN medium decreases ROE's spectral aberrations.<sup>[22–25]</sup> However, practical challenges in manufacturing, such as spatial resolution and complexity of GRIN profiles in a 3D volume of ROEs, limit the extent to which chromatic aberrations can be removed. Micro-gratings as a category of thin DOEs can offer unique opportunities as an alternative to these issues. DOEs can be engineered to exhibit a negative refractive index dispersion which causes their focal length to increase with wavelength.<sup>[32–34]</sup> Therefore, layers consisting of DOE and ROE are expected to cancel out their opposite-signed deviations of focal point, thereby effectively realizing achromatic optics.<sup>[35]</sup> Furthermore, DOEs facilitate arbitrary phase maps via tailoring their unit cell geometry and/or spacing, which makes it possible to correct both chromatic and monochromatic aberrations, potentially reducing the total number of components in an optical system.<sup>[36]</sup> With the versatile manufacturability of our novel process on both flat and non-flat optical platforms, photochemically induced DOEs are poised to be competitive as part of hybrid DOE–ROFs for the realization of aberration-compensated optics with substantially reduced size, weight, and power consumption factor.

To demonstrate the viability of photochemically induced micro-gratings as DOEs, a series of surface structures were computationally designed and experimentally assessed. A choice of grid spacings and laser wavelengths was made to be identical in computational and experimental tests for a direct comparison. Specifically, transmission grid structures with areas up to

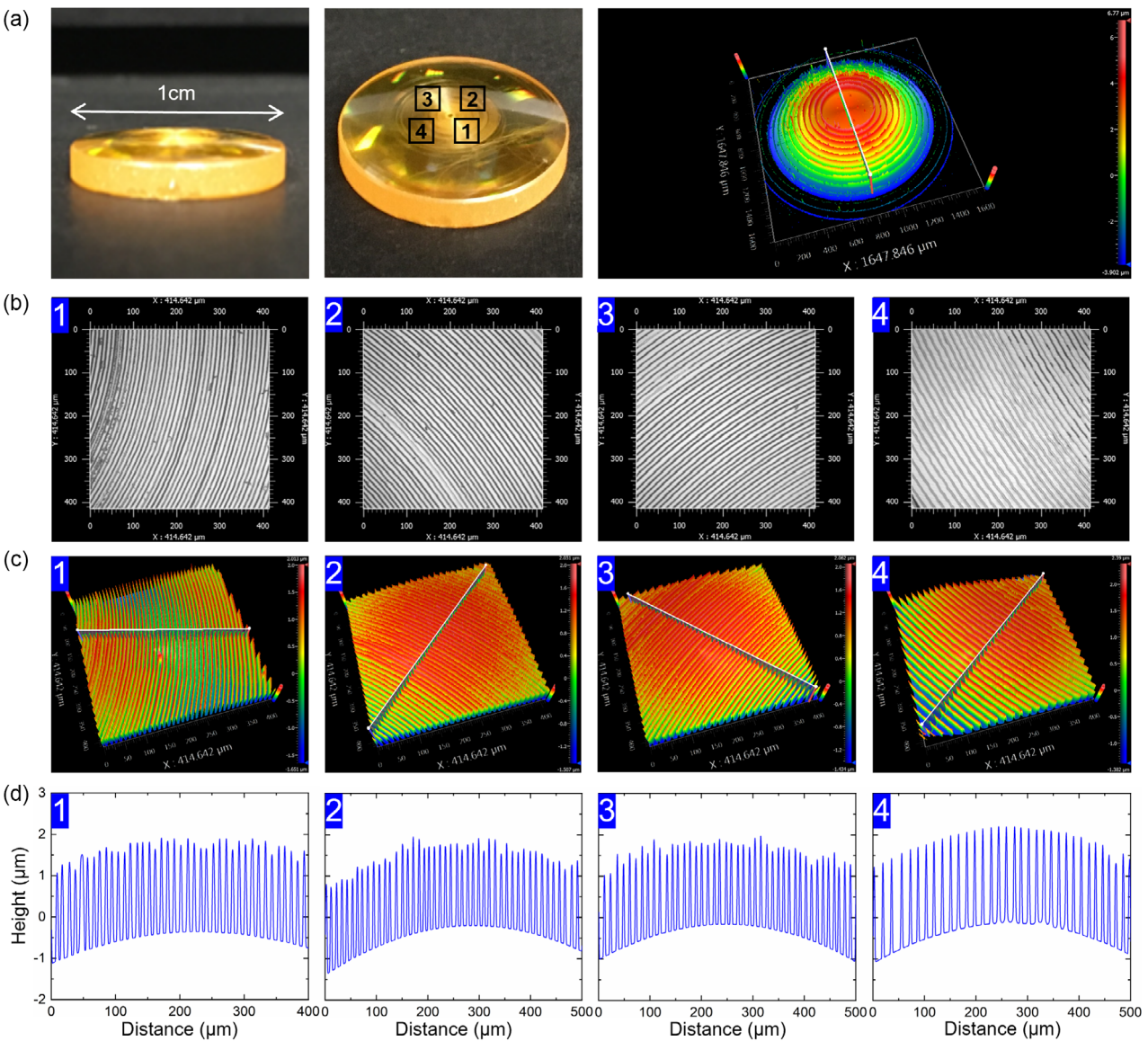


**Figure 4.** a) Photographs of plano-convex ZnSe substrate. b) Large-area ( $\approx 1.65 \times 1.65 \text{ mm}^2$ ) WLI images of photochemically created concentric rings on the curved ZnSe substrate. c) WLI images of four representative local regions of the concentric rings. d) Corresponding height profiles of the four regions.

$5 \times 5 \text{ mm}^2$  and a wide range of wall-to-wall spacings from 5 to  $20 \mu\text{m}$  were subjected to incident infrared laser beams with wavelengths ranging from 2 to  $10 \mu\text{m}$ . These structures were first simulated using a COMSOL Multiphysics code. The height of individual walls was set to be  $3.5 \mu\text{m}$  while their bottom width and aspect ratio, which reproducibly change as a function of spacing, were adopted from those of experimentally created surface micro-gratings. Specific parameters for the simulation are described in Experimental Section. **Figure 5b–i** shows examples for both modeled and photochemically induced grids with a spacing of  $5 \mu\text{m}$  subjected to laser beam with a wavelength of  $4 \mu\text{m}$  as well as their resulting diffraction intensity profiles in a transmissive mode. The same types of data were created for all combinational cases to extract total simulated and experimental diffraction efficiencies in each set of spacing-wavelength

parameters, using an equation of  $\eta = \frac{\sum P_{(n,k)} - P_{(0,0)}}{P_i}$ , where  $\eta$ ,  $P_{(n,k)}$ ,  $P_{(0,0)}$ , and  $P_i$  are the total diffraction efficiency,  $(n,k)$ th diffraction-order power, transmitted power, and incident power, respectively.<sup>[4,37,38]</sup>

The simulated and experimental total diffraction efficiencies are plotted as a function of wavelength, as shown in **Figure 5j,k**, respectively. Here, the impact of laser wavelength on the diffraction efficiency of grids with a specific spacing exhibits a clear trend in both simulated and experimental tests. Specifically, for a spacing of  $5 \mu\text{m}$  as an example in **Figure 5j, k**, an increase in laser wavelength from 2 to  $4 \mu\text{m}$  results in an increase in simulated and experimentally measured diffraction efficiencies up to maximum values, respectively. A further increase in laser wavelength beyond  $4 \mu\text{m}$  involves a decrease in

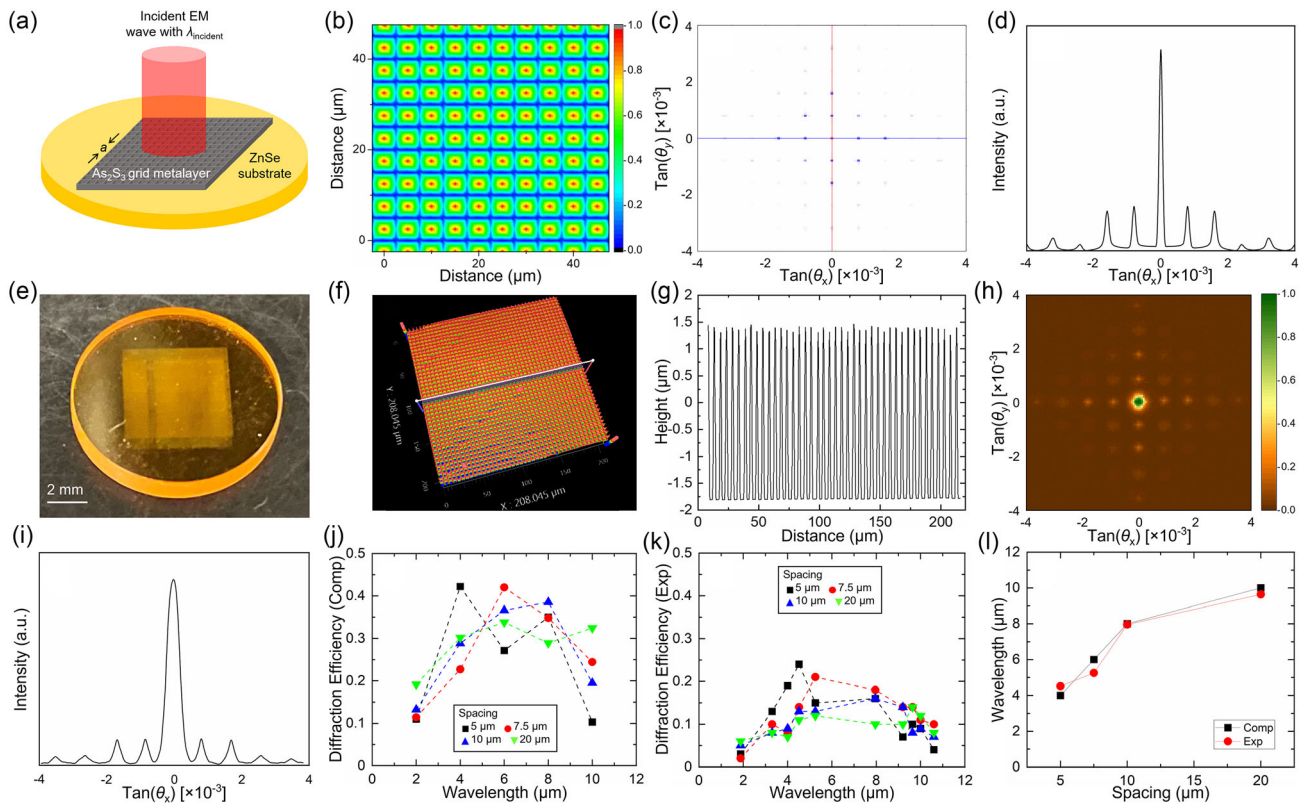


**Figure 5.** a) A schematic of a grid micro-grating subjected to incident laser beam. b) The field distribution of a COMSOL-created grid structure with a spacing of  $5\ \mu\text{m}$  subjected to a laser beam with a wavelength of  $4\ \mu\text{m}$ . c) Simulated diffraction spots. d) Extracted spatial intensity profiles of spots in (c). e) Photograph of a photochemically created grid micro-grating. f) WLI image of the structure. g) Extracted height profile of the structure. h) Experimental diffraction spots. i) Extracted spatial intensity profiles of spots in (h). j) Simulated total diffraction efficiency for each spacing as a function of wavelength. k) Experimental total diffraction efficiency for each spacing as a function of wavelength. l) Spacing–wavelength correlation corresponding to maximum computed and experimental diffraction efficiencies.

the efficiencies. There is a trend where a wavelength leading to a maximum diffraction efficiency increases with spacing. To illustrate this, the wavelength-spacing parameters leading to maximum diffraction efficiencies are plotted in Figure 5l where the spacing-dependent monotonic increase in wavelength is consistent between computational and experimental tests, indicating spacing-dependent optical tailorability.<sup>[37,38]</sup> It is also noteworthy that the discrepancy in absolute magnitudes between theoretical and experimental diffraction efficiencies is likely associated with topographical imperfections such as 1) the statistically varying fidelity of individual walls and 2) their surface defects within grid structures, both of which give rise to variance of the laser beam’s diffracted intensities. The universal trend and consistency observed in simulated and experimental results strongly indicate that our novel photochemical process provides a well-defined process–structure–property relationship, thereby being capable of creating spatially tunable and optically functional surface micro-gratings as a form of DOEs.

## 6. Conclusion and Outlook

In summary, we have developed a novel photochemical process for the fabrication of spatially tailorable  $\text{As}_2\text{S}_3$  surface

micro-gratings and demonstrated their optical function as DOEs. Our DLW process uses near-bandgap laser irradiation that structurally reorganizes thermally deposited chalcogenide glasses such that subsequent chemical-etching reveals structures of our written patterns. A combined simulation-experimental approach to the design and realization of surface micro-gratings as infrared DOEs has proved that our photochemically engineered structures are optically functional. For the first time, we have demonstrated that our process can create micro-gratings on curved substrates. The compatibility of our photochemical process with conformal writing enables fabrication of grating-based DOEs on curved refractive substrates to potentially create aberration-corrected hybrid diffractive–refractive lenses. We believe that the flexibility of our process and resulting optical functionality of our created DOEs provide a glimpse into our vision for thin hybrid diffractive–refractive infrared components that could rival or even exceed the performance of traditional bulky optics. To identify whether the tunability of our resulting micro-gratings and fidelity of their individual walls can be further optimized, endeavors to explore additional aspects of our DLW and post etching processes are in progress. We have ongoing work to assess hybrid components’ aberration correction performance by integrating photochemically created DOEs on the

surface of ROEs where the spectral dispersion of electromagnetic waves going through a hybrid diffractive–refractive component will be quantitatively compared with those going through an ROE itself (i.e., without a DOE on it). The successful realization and assessment of such hybrid structures would fully demonstrate our approach's advantage.

## 7. Experimental Section

**Source Material Fabrication:** Bulk chalcogenide glasses of  $As_2S_3$  were prepared by a conventional melt-quenching technique. All glasses were made using high-purity raw materials from Alfa-Aesar: As (99.999%) and S (99.999%). These elements were carefully weighed and batched in a nitrogen-purged MBraun Labmaster 130 glove box. The weighed batches (50 g) were loaded into cleaned fused quartz tubes and sealed under vacuum using a methane-oxygen torch to form sealed ampoules. The batches were melted in a rocking furnace overnight at a high temperature of 850 °C. After overnight rocking at the temperature, the furnace was cooled down to the quench temperature of 650 °C, prior to removal from the furnace for quenching using compressed air flowing over the ampoule. The quench rate for this method was estimated to be  $\approx 120\text{ °C min}^{-1}$ .

**Film Deposition:** Thin films of  $As_2S_3$  were deposited using thermal evaporation from a single  $As_2S_3$  source. The ZnSe substrates were cleaned by 5 min sonication in acetone, rinsed in isopropyl alcohol, and blow-dried with  $N_2$  gas. They were then subjected to 10 min of  $O_2$  plasma and immediately transferred to the deposition chamber. The film deposition was performed using a custom-designed system (PVD Products, Inc.) following previously established protocols.<sup>[28]</sup> Since the target thickness is large (2–3.5  $\mu\text{m}$ ), they were deposited in multiple runs with cooling in between to reduce residual stress. The substrate temperature was measured by a thermocouple throughout the deposition process. Stoichiometries of the films were confirmed using wavelength-dispersive spectroscopy on a JEOL JXA-8200 SuperProbe Electron Probe Microanalyzer to be within 2% (atomic fraction) deviation from target compositions.

**DLW:** A Mai Tai Ti:sapphire laser with a center wavelength of 801 nm, a repetition frequency of 80 MHz, and a pulse width of  $<100\text{ fs}$  was used for DLW in  $As_2S_3$  films. The beam was passed through a variable attenuator to control the average power and a shutter. Process parameters including sub-ablation powers of 24–40 mW and scan speed of 0.125–0.250  $\text{mm s}^{-1}$  were explored to maximize cross-linking of atomic bonds along paths of grids, parallel walls, concentric rings, and pillars within films. The beam was focused using either a  $50\times/0.55\text{ NA}$  or  $100\times/0.75\text{ NA}$  objective onto the  $As_2S_3$  films. The substrates were secured onto a Physik Instrumente H-840 6-Axis Hexapod (programmable stage), and a camera was used to image the plane of samples during irradiation. The entire system was controlled by a LabVIEW program that automates the laser writing of pre-designed patterns.

**Post Chemical Etching:** DIPA of 0.4–0.6 mol% was mixed with DMSO in beakers using a magnetic stirrer. Subsequently, a laser-processed specimen was immersed in the solvent for a variety of durations up to 1 h. The selectively dissolved specimen was then transferred to another fresh solution of 0.5 mol% DIPA in DMSO and etched for 1 min to further dissolve any possibly existing residues in inter-structure gaps. Finally, the specimen was rinsed in acetone for 3 min to wash away DIPA-DMSO solvent remaining on the surface of specimens. The introduction and removal of specimens was carried out at a rate of  $\approx 1\text{ mm s}^{-1}$ . Also, specimens remained still while etching was underway. These two protocols were intended to minimize a friction between a specimen and a solvent, thereby avoiding the destruction of micro-gratings. During the etching process, beakers were covered with aluminum foils to avoid evaporation of the solvent which would disrupt the original mixing ratio and its etching behavior. Upon the completion of etching, specimens were dried in a desiccator for 1 h to get them ready for characterizations.

**Structural Characterizations:** For the identification of pre- and postirradiation molecular structure of the films, a Horiba Jobin Yvon confocal

micro-Raman system with an excitation wavelength of 785 nm was used. The beam was focused by a  $100\times/0.75\text{ NA}$  objective, and the Raman signals were collected for 60 s in a raster scan mode with a writing velocity of 0.25  $\text{mm s}^{-1}$  and intervals of 5  $\mu\text{m}$ . The optical power was reduced to 60% by an optical density filter to prevent any undesired photo-induced change to the films. For the characterization of topography, ZYGO 6300 WLI was used. Along with a variety of lenses with physical and digital magnifications from  $5\times$  to  $50\times$  and  $0.5\times$  to  $2.0\times$ , respectively, areas from  $80\times 80$  to  $3200\times 3200\text{ }\mu\text{m}^2$  were scanned to visualize the topography of the surface micro-gratings in 3D.

**Optical Characterizations:** For the experimental assessment of photochemically created surface micro-gratings' optical functionality as DOEs, we launched the laser beam into the structures and observed their diffraction beam orders in a transmission mode. Specifically, Gaussian single-mode laser beam with central wavelengths of  $\approx 1.88$  to 10.6  $\mu\text{m}$ , bandwidths of  $\approx 30$ –40 nm, and  $1/e^2$  diameters of  $\approx 4$  to 5 mm was focused through a Newport KBX061 biconvex lens with a focal length of  $\approx 88\text{ mm}$  and formed a beam spot with a diameter of  $\approx 300\text{ }\mu\text{m}$  and an input NA of 0.05 as the beam hit the surface of specimens. Resulting diffraction patterns were monitored and recorded using a Pyrocam IIIHR Beam Profiling Camera.

**Optical Design:** The finite-element method implemented by COMSOL Multiphysics was used to build full-wave simulations of surface grid structures. The materials of the surface grid structures and their underlying substrate were specified by the optical constants and dimensions of  $As_2S_3$  and ZnSe, respectively. The diffraction efficiencies of multiple transmittance orders were determined by calculating the scattering parameters (S-parameters) of an incident electromagnetic wave in the ports of the model. In the simulation, Floquet periodic boundary conditions were used for the 3D unit cell of the surface grid structures. The spatial intensity distribution of the diffraction orders (the spot diagram of diffraction orders) was obtained by simulating the Gaussian beam propagation through the surface grid structures in the Ray Optics Module. In the module, S-parameters for the unit cell of the surface grid structures obtained from the electromagnetic waves, frequency domain interface were used by the geometrical optics interface, to quantify the transmittance of each diffraction order.

## Supporting Information

Supporting Information is available from the Wiley Online Library or from the author.

## Acknowledgements

M.K., B.M.T., and M.Y.S. equally contributed to this work. This work was funded by Defense Advanced Research Projects Agency Defense Sciences Office Program: EXTREME Optics and Imaging under agreement no. HR00111720029. The views, opinions, and/or findings expressed are those of the authors and should not be interpreted as representing the official views or policies of the Department of Defense. The authors thank L. Li and J. Qin at Massachusetts Institute of Technology for assisting in  $As_2S_3$  film deposition as well as D. J. McGill and A. Kirk at Lockheed Martin Corporation for assisting in DLW. The authors also thank J. Hallett at the University of Central Florida for assisting in post chemical etching.

## Conflict of Interest

The authors declare no conflict of interest.

## Data Availability Statement

The data that support the findings of this study are available from the corresponding author upon reasonable request.



## Keywords

arsenic sulfide, chalcogenide glasses, diffraction optical elements, direct laser writing, micro-gratings, selective etching

Received: August 22, 2023

Revised: September 26, 2023

Published online: October 11, 2023

- [1] T. D. Cope, *J. Franklin Inst.* **1932**, 214, 99.
- [2] J. Strong, *Vistas Astron.* **1986**, 29, 137.
- [3] G. A. Harrison, E. G. Loewen, R. S. Wiley, *Appl. Opt.* **1976**, 15, 971.
- [4] C. Palmer, *Diffraction Grating Handbook*, Richardson Grating Laboratory, New York **2000**.
- [5] M. Kozák, J. McNeur, K. J. Leedle, H. Deng, N. Schönerberger, A. Ruehl, I. Hartl, J. S. Harris, R. L. Byer, P. Hommelhoff, *Nat. Commun.* **2017**, 8, 14342.
- [6] Q. Jia, X. Ou, M. Langer, B. Schreiber, J. Grenzer, P. F. Siles, R. D. Rodriguez, K. Huang, Y. Yuan, A. Heidarian, R. Hübner, T. You, W. Yu, K. Lenz, J. Lindner, X. Wang, S. Facsko, *Nano Res.* **2017**, 11, 3519.
- [7] H. Miao, A. A. Gomella, N. Chedid, L. Chen, H. Wen, *Nano Lett.* **2014**, 14, 3453.
- [8] S. Chen, Y. Huang, D. Visser, S. Anand, I. A. Buyanova, W. M. Chen, *Nat. Commun.* **2018**, 9, 3575.
- [9] X. Miao, K. Chabak, C. Zhang, P. K. Mohseni, D. Walker Jr., X. Li, *Nano Lett.* **2015**, 15, 2780.
- [10] R. Liu, X. Zhao, C. Roberts, L. Yu, P. K. Mohseni, X. Li, V. Podolskiy, D. Wasserman, *Adv. Mater.* **2016**, 28, 1441.
- [11] A. Flores, M. R. Wang, J. J. Yang, *Appl. Opt.* **2004**, 43, 5618.
- [12] G. Xue, Q. Zhai, H. Lu, Q. Zhou, K. Ni, L. Lin, X. Wang, X. Li, *Microsyst. Nanoeng.* **2021**, 7, 31.
- [13] Y. Wang, J.-A. Pan, H. Wu, D. V. Talapin, *ACS Nano* **2019**, 13, 13917.
- [14] K. Li, J. Li, C. Reardon, C. S. Schuster, Y. Wang, G. J. Triggs, N. Damnik, J. Muenchenberger, X. Wang, E. R. Martins, T. F. Krauss, *Sci. Rep.* **2016**, 6, 32945.
- [15] T. J. Kempa, D. K. Bediako, S.-K. Kim, H.-G. Park, D. G. Nocera, *Proc. Natl. Acad. Sci. USA* **2015**, 112, 5309.
- [16] M. Kang, R. S. Goldman, *Appl. Phys. Rev.* **2019**, 6, 041307.
- [17] Q. Huang, Q. Jia, J. Feng, H. Huang, X. Yang, J. Grenzer, K. Huang, S. Zhang, J. Lin, H. Zhou, T. You, W. Yu, S. Facsko, P. Jonnard, M. Wu, A. Giglia, Z. Zhang, Z. Liu, Z. Wang, X. Wang, X. Ou, *Nat. Commun.* **2019**, 10, 2437.
- [18] M. Kang, T. W. Saucer, M. V. Warren, J. H. Wu, H. Sun, V. Sih, R. S. Goldman, *Appl. Phys. Lett.* **2012**, 101, 081905.
- [19] B. AlQattan, A. K. Yetisen, H. Butt, *ACS Nano* **2018**, 12, 5130.
- [20] T. Gissibl, S. Thiele, A. Herkommer, H. Giessen, *Nat. Photonics* **2016**, 10, 554.
- [21] C. R. Ocier, C. A. Richards, D. A. Bacon-Brown, Q. Ding, R. Kumar, T. J. Garcia, J. van de Groep, J.-H. Song, A. J. Cyphersmith, A. Rhode, A. N. Perry, A. J. Littlefield, J. Zhu, D. Xie, H. Gao, J. F. Messinger, M. L. Brongersma, K. C. Toussaint Jr., L. L. Goddard, P. V. Braun, *Light Sci. Appl.* **2020**, 9, 196.
- [22] M. Kang, A. M. Swisher, A. V. Pogrebnyakov, L. Liu, A. Kirk, S. Aiken, L. Sisken, C. Lonergan, J. Cook, T. Malendevych, F. Kompan, I. Divliansky, L. B. Glebov, M. C. Richardson, C. Rivero-Baleine, C. G. Pantano, T. S. Mayer, K. Richardson, *Adv. Mater.* **2018**, 30, 1803628.
- [23] L. Sisken, M. Kang, J. M. Veras, C. Smith, A. Buff, A. Yadav, D. McClane, C. Blanco, C. Rivero-Baleine, T. S. Mayer, K. Richardson, *Adv. Funct. Mater.* **2019**, 29, 1902217.
- [24] I. Mingareev, M. Kang, M. Truman, J. Qin, G. Yin, J. Hu, C. M. Schwarz, I. B. Murray, M. C. Richardson, K. A. Richardson, *Opt. Laser Technol.* **2020**, 126, 106058.
- [25] P. S. Shirshnev, M. Kang, I. Divliansky, K. A. Richardson, L. B. Glebov, *Opt. Mater. Express* **2022**, 12, 3429.
- [26] A. Zoubir, M. Richardson, C. Rivero, A. Schulte, C. Lopez, K. Richardson, N. Ho, R. Vallee, *Opt. Lett.* **2004**, 29, 748.
- [27] C. M. Schwarz, S. M. Kuebler, C. Rivero-Baleine, B. Triplett, M. Kang, Q. Altemose, C. Blanco, K. A. Richardson, Q. Du, S. Deckoff-Jones, J. Hu, Y. Zhang, Y. Pan, C. Rios, *J. Opt. Microsyst.* **2021**, 1, 013502.
- [28] C. Goncalves, M. Kang, B.-U. Sohn, G. Yin, J. Hu, D. T. H. Tan, K. Richardson, *Appl. Sci.* **2018**, 8, 2082.
- [29] G. C. Chern, I. Lauks, *J. Appl. Phys.* **1982**, 53, 6979.
- [30] Y. Zha, M. Waldmann, C. B. Arnold, *Opt. Mater. Express* **2013**, 3, 1259.
- [31] S. Wong, M. Deubel, F. Perez-Willard, S. John, G. A. Ozin, M. Wegener, G. von Freymann, *Adv. Mater.* **2006**, 18, 265.
- [32] E. Nicoletti, D. Bulla, B. Luther-Davies, M. Gu, *Appl. Phys. B* **2011**, 105, 847.
- [33] T. Stone, N. George, *Appl. Opt.* **1988**, 27, 2960.
- [34] C. J. Zapata-Rodriguez, M. T. Caballero, *Opt. Lett.* **2007**, 32, 2472.
- [35] W. T. Chen, A. Y. Zhu, J. Sisler, Y.-W. Huang, K. M. A. Yousef, E. Lee, C.-W. Qiu, F. Capasso, *Nano Lett.* **2018**, 18, 7801.
- [36] R. Sawant, D. Andren, R. J. Martins, S. Khadir, R. Verre, M. Kall, P. Genevet, *Optica* **2021**, 8, 1405.
- [37] S. Wise, V. Quetschke, A. J. Deshpande, G. Mueller, D. H. Reitze, D. B. Tanner, B. F. Whiting, Y. Chen, A. Tunnermann, E. Kley, T. Clausnitzer, *Phys. Rev. Lett.* **2005**, 95, 013901.
- [38] A. Patri, S. Kena-Cohen, C. Caloz, *ACS Photonics* **2019**, 6, 3298.